

1 **Formation and evolution of the large-scale magnetic fields in Venus Ionosphere: Results**
2 **from a 3D global multi-species MHD model**

3 Yingjuan Ma¹, Gabor Toth², Andrew F. Nagy², Janet Luhmann³, C.T. Russell¹
4

5 ¹Department of Earth, Planetary, and Space Sciences, UCLA, Los Angeles, CA, 90025, United
6 States ²Department of Climate and Space Sciences and Engineering, University of Michigan,
7 Ann Arbor, MI, 48109, United States ³Space Sciences Laboratory, University of California,
8 Berkeley, CA 94720
9

10
11
12 Main points of the paper:

- 13 • The global MHD model self-consistently reproduces the formation and evolution of the
14 large-scale magnetic fields in the Venus ionosphere.
- 15 • Model results show that it takes quite long time (~ hours) for the magnetic field to
16 penetrate into and decay in the ionosphere.
- 17 • The large-scale magnetic fields in the ionosphere act as an additional obstacle to the solar
18 wind

19 **Plain language Summary**

20 Large-scale magnetic fields have been observed at Venus' ionosphere by previous Venus
21 missions. In this study, we examine the formation and evolution of the large-scale magnetic field
22 in the Venus ionosphere using a sophisticated global model. A time-dependent model run is
23 performed under varying solar wind dynamic pressure (density). Model results show that the
24 outside interaction region responds quickly (~ minutes) to the solar wind variation, while the
25 response time of the ionosphere is long (~ hours). We also found that the ion escape rate has a
26 non-linear response to the change of solar wind dynamic pressure.
27
28

This is the author manuscript accepted for publication and has undergone full peer review but has not been through the copyediting, typesetting, pagination and proofreading process, which may lead to differences between this version and the Version of Record. Please cite this article as doi: [10.1029/2020GL087593](https://doi.org/10.1029/2020GL087593)

29 ABSTRACT

30 Large-scale magnetic fields have been observed in Venus' ionosphere by both the Pioneer Venus
31 Orbiter (PVO) and Venus Express spacecraft. In this study, we examine the formation and
32 evolution of the large-scale magnetic field in the Venus ionosphere using a sophisticated global
33 multi-species MHD model that has been developed for Venus [Ma *et al.*, 2013]. A time-
34 dependent model run is performed under varying solar wind dynamic pressure. Based on model
35 results, we find that: 1) the initial response of the induced magnetosphere is fast (~ minutes); 2) a
36 large-scale magnetic field gradually forms in the ionosphere when the solar wind dynamic
37 pressure suddenly exceeds the ionospheric thermal pressure; 3) both the penetration and decay of
38 the large-scale magnetic field in the ionosphere are slow (~ hours); 4) the ion escape rate has a
39 non-linear response to the change of solar wind dynamic pressure.
40

41 1. Introduction

42 PVO observations have shown clear evidence that Venus has no significant global intrinsic
43 field [Phillips and Russell, 1987]. As a result, its atmosphere and ionosphere interact with the
44 solar wind much more directly, in contrast to Earth [Cravens *et al.*, 2013; Futaana *et al.*, 2017].
45 PVO observations have also shown that Venus' ionosphere has two distinct states: magnetized
46 and un-magnetized, commonly thought to be controlled by the relative strength of the solar wind
47 dynamic pressure and ionosphere thermal pressure [Cravens *et al.*, 2013]. During solar
48 maximum conditions, the ionospheric thermal pressure is normally stronger than the solar wind
49 dynamic pressure, and the ionosphere is often found to be in the un-magnetized state, due to the
50 high electrically conducting property of the ionosphere, which enables a strong current to fully
51 stop the penetration of the induced magnetic field. During solar minimum conditions, the solar
52 wind dynamic pressure is normally larger than the ionospheric thermal pressure. Thus, the
53 induced magnetic field could at least partially penetrate into the ionosphere, resulting in a
54 magnetized ionosphere. Such a scenario was first confirmed using self-consistent global MHD
55 models by Ma *et al.* [2013], under steady-state solar wind conditions. As both the upstream solar
56 wind conditions and solar EUV flux constantly vary with time, the relative strength of the solar
57 wind dynamic pressure and the ionospheric thermal pressure could also vary. Thus, the state of
58 the ionosphere is expected to change from one to the other in response to variations of external
59 drivers, especially solar wind dynamic pressure. A clear example of such change is shown by
60 PVO observations for three consecutive orbits: 175, 176 and 177 [Elphic *et al.*, 1980]. However,
61 how the ionosphere changes from one state to another has not been fully understood, due to
62 limitations of single spacecraft observations.
63

64 The magnetic field profiles in the magnetized ionosphere are far from uniform. A large-scale
65 magnetic field (sometimes called low altitude magnetic belt) was found in the dayside
66 ionosphere in both PVO and VEX observations [Luhmann *et al.*, 1980; Russell *et al.*, 1983;
67 Villarreal *et al.*, 2015]. These large-scale fields are mainly horizontal, and usually show a
68 distinct minimum near ~200 km altitude [Luhmann *et al.*, 1980]. Russell *et al.* [1983] first
69 suggested that time variations are essential to explaining the observed features of the low altitude
70 magnetic belt, as the observations of the large-scale magnetic field likely occurred sometime
71 after it had been created and evolved. The evolution of large-scale fields has been studied by
72 Luhmann *et al.* [1984], Cravens *et al.* [1984], and Cloutier [1984], using various one-
73 dimensional approaches, solving mainly the magnetic diffusion equation and the estimated decay
74 time scale ranges from 2-3 minutes [Cloutier, 1984] to between 10 min to a few hours,

75 depending on assumptions on vertical velocities [Cravens *et al.* 1984]. Later, more
76 comprehensive 1D and 2D multi-species MHD models were developed for Venus by Shinagawa
77 and co-authors [Shinagawa *et al.*, 1987, 1991; Shinagawa and Cravens, 1988; Shinagawa, 1996a,
78 1996b], which were able to reproduce many observed features below 250 km altitude, including
79 the electron density “ledge” near 190 km altitude and a decrease of magnetic field around 200
80 km altitude. However, significant disagreement between the calculated and observed plasma
81 densities at high altitudes suggested that a 3D global model is needed to understand the
82 formation and the evolution of the large-scale magnetic fields in the Venus ionosphere, due to
83 the three-dimensional nature of the solar wind interaction with the Venus ionosphere.
84

85 In addition, previous statistical studies have found a positive correlation between ion escape rates
86 and upstream solar wind dynamic pressure [Luhmann *et al.*, 2007; Edberg *et al.*, 2011].
87 However, there is little understanding of the ionospheric responses to solar wind variations, due
88 to the lack of coordinated observations of both upstream solar wind conditions and simultaneous
89 plasma properties in the Venus ionosphere. In this paper, we use a sophisticated multi-species
90 MHD model developed for Venus [Ma *et al.*, 2013], to characterize the changes of the
91 ionosphere and the induced magnetosphere under varying solar wind dynamic pressure. This
92 model enables us to answer the question of how the ionosphere changes from one state to another.
93 We briefly describe the model used for the study in Section 2. The model results are present in
94 Section 3, followed by discussion and summary in Section 4.
95

96 2. Time-dependent global multi-species MHD model

97
98 The multi-species global MHD model of Venus based on the BATS-R-US code [Toth *et al.* 2012]
99 is described in detail in Ma *et al.* [2013]. Model results of three cases are presented in Ma *et al.*
100 [2013], corresponding to solar max, solar min, and a Venus Express (VEX) case, which are in
101 good agreement with the observations of both PVO and VEX in terms of both bow shock
102 locations and magnetic field observations. The model solves continuity equations of multiple ion
103 species for H^+ , O^+ , O_2^+ and CO_2^+ , and momentum and energy, and magnetic field induction
104 equations. The simulation uses the Venus Solar Orbital (VSO) coordinates, with a computational
105 domain of $-24R_V \leq X \leq 8R_V$, $-16R_V \leq Y$, $Z \leq 16R_V$, where $R_V = 6052$ km is the radius of Venus.
106 The inner boundary was taken to be 100 km above the Venus surface in a collision-dominated
107 region, and thus we assume ion densities are in photochemical equilibrium. The inner boundary
108 conditions for U and B are the same as described in Ma *et al.*, [2013], assuming zero gradients of
109 both vectors. The angular resolution is kept at 2.5° , both azimuthally and longitudinally in the
110 computation domain. The radial resolution is 5 km ($\sim 0.0008 R_V$) from the lower boundary
111 (100km) to 500 km altitude; above this altitude, the radial resolution gradually increases from 5
112 km to 2000 km ($0.34 R_V$) near the outer boundary at $24 R_V$ downstream. Such a grid contains
113 $480 \times 144 \times 72$ (about 5 million) cells in total. Ionospheric conductivity is included in the model,
114 and is calculated in the same way as described in Ma *et al.*, [2013].
115

116 To understand the formation and evolution of the large-scale magnetic field in the Venus
117 ionosphere, we run an idealized solar wind dynamic pressure enhancement event with time-
118 varying solar wind conditions. In the event, the dynamic pressure enhancement is realized by
119 changing only the solar wind density, with all the other input parameters unchanged. We first run
120 the model under quiet solar wind conditions for 1 hour to reach a quasi-steady state, and then

121 enhance the solar wind density by a factor of 2, which lasts for 2 hours, as shown in Figure 1a.
122 The density then returns to quiet conditions for two hours, with a total simulation time of 5 hours.
123 The quiet solar wind condition is taken to be the same as in case 1 (solarmax case) of *Ma et al.*
124 [2013], with $n_{\text{SW}} = 17 \text{ cm}^{-3}$; $U = -400 \text{ km/s}$, $B_{\text{MF}} = [12.1, -8.8, 0] \text{ nT}$, and $T_{\text{SW}} = 2.5 \times 10^5 \text{ K}$. The
125 corresponding solar wind dynamic pressure is 4.5 nPa, and the fast magnetosonic Mach number
126 is 4.2. The neutral density and EUV flux are also set for solar maximum conditions. The
127 disturbed solar wind propagates into the simulation domain from the upstream outer boundary at
128 $X = -8 R_V$. This is an idealized event of a dynamic pressure pulse. In reality, the density, velocity
129 and magnetic field could all vary. However, it could be challenging to distinguish causes and
130 consequences, as the impacts of these parameters are mixed. In this sense, simple events are
131 more useful in probing the physical processes in the Venus-solar wind interaction. The
132 simulation results of the event are presented in the next section.

133 134 3. Model results

135 The variation of the ion escape rates during this ideal solar wind density pulse event is calculated
136 through integrating the net ion fluxes through the $5 R_V$ sphere and is shown in Figure 1b (solid
137 lines). For solar maximum conditions, the O^+ ion is by far the most dominant ion escaping from
138 Venus. Note that the CO_2^+ escape flux is about 5 orders smaller than O^+ , less than 1×10^{21} (not
139 shown in the figures). To highlight the changes of escape rates due to varying solar wind
140 conditions, we also plot the escape rates in dashed lines for the baseline case, using constant
141 solar wind conditions for reference. The total ion escape rate for quiet solar wind conditions
142 averaged over 4 hours (1 hour - 5 hour) is around 8×10^{25} particles/s, and the corresponding mass
143 loss is $\sim 2.14 \text{ kg/s}$. During the two-hour period of high solar wind dynamic pressure, the O^+
144 escape rate increased about 49.6% on average. The ion escape rates are still significantly high,
145 especially for the first 30 minutes after the density pulse. The O^+ loss rate is still 27% higher on
146 average for the first hour (between 3-4 hours). The ion escape rates produced by the model for
147 solar maximum under quiet solar wind conditions is consistent with the value estimated by *Brace*
148 *et al.* [1987], 5×10^{25} particles/s, but much larger than the $\sim 1 \times 10^{25}$ particles/s estimated by
149 *McComas et al.* [1986], both using PVO observations. The escape rates are also much larger than
150 2.7×10^{24} particles/s, estimated for solar minimum conditions using Venus Express observations
151 [*Fedorov et al.*, 2011]. The large enhancement of the ion escape rate at times of high solar wind
152 dynamic pressure is consistent with findings of *Luhmann et al.* [2007].

153
154 The rest of the panels in Figure 1 illustrate how the interaction changes globally during the
155 density pulse event. Panels c1-c3 show plasma velocity distribution in the XZ plane at 1 hour, 3
156 hour and 5 hour, corresponding to quiet time, under enhanced solar wind density and two hours
157 after the solar wind returned to quiet conditions, respectively. The bow shock locations from the
158 model at quiet solar wind conditions, both at 1 hour and 5 hour, match very well with the mean
159 bow shock locations for solar maximum [*Zhang et al.* 1990], except they are closer to the planet
160 near the subsolar region and farther away near the flank regions. This is because the bow shock
161 fitting function assumed that the bow shock locations are axial symmetric, while in reality, the
162 bow shock locations are asymmetric in the terminator plane, farther away from the planet in the
163 direction perpendicular to the magnetic field (in the Z direction), compared with the parallel
164 direction (Y direction), as observed by PVO [*Russell et al.*, 1988]. At 3 hour, when the solar
165 wind dynamic pressure is high, the bow shock locations are significantly compressed. The
166 bottom panels show corresponding magnetic field strength contour plots. There is a clear

167 magnetic field enhancement (induced magnetosphere) near the planet. Also, the peak magnetic
168 field is the highest at 3 hour, as expected. To show clearly the different magnetic state of the
169 ionosphere, we also showed zoom-in views of the magnetic field strength inside the region of
170 $0.72R_V < X < 1.12R_V$, and $0.3 R_V < Z < 0.7 R_V$ (panels d1-d3). As can be clearly seen, the ionosphere
171 is in the unmagnetized state at 1 hour, strongly magnetized state at 3 hour and there is a low
172 altitude magnetic belt in the ionosphere at 5 hour. The peak magnetic field are 115 nT, 98 nT, 34
173 nT and 27 nT at 0, 30, 60 and 90 SZA, respectively at 3 hour (see figure S1). The magnetic fields
174 in the low altitude belt are weaker at large SZA, consistent with PVO observations [Luhmann *et*
175 *al.*, 1980].

176
177 To examine in more detail how the Venus space environment responds to the density (pressure)
178 pulse event, we also plotted the snapshots of various pressure profiles along the subsolar line for
179 different times, as shown in Figure 2. In each panel, pressure profiles of thermal pressure (in
180 blue), dynamic pressure (in red), magnetic pressure (green) and total pressure (black) are plotted.
181 Before the pressure pulse reaches Venus, solar wind dynamic pressure (~ 4.5 nPa) is smaller than
182 the peak of the ionospheric thermal pressure (~ 8.2 nPa), and the Venus ionosphere is
183 unmagnetized and dominated by thermal pressure (see panel a). It takes about 1 min and 40 s for
184 the pressure pulse to propagate from the outer boundary to the Venus bow shock locations (see
185 panel b), and the solar wind dynamic pressure doubles outside of the bow shock due to
186 enhancement of the solar wind density. The high solar wind dynamic pressure pushes the bow
187 shock location from $1.4 R_V$ inward all the way to $1.3 R_V$, in less than 20 seconds (see panel c).
188 Across the shock, the solar wind dynamic pressure is converted mostly to thermal pressure in the
189 sheath region, so the thermal pressure inside the shock increases nearly by a factor of two,
190 shortly after the pressure pulse arrival. Closer to the planet, the peak magnetic pressure also
191 doubles in the induced magnetosphere (IM). Both the magnetosheath region and IM respond
192 quickly to the enhanced solar wind dynamic pressure in 10s of seconds. The predicted timescale
193 is similar to the recovery timescale of the Martian magnetosphere to IMF variations as estimated
194 by a hybrid model [Romanelli *et al.*, 2019]. The bow shock locations bounce back a little and
195 settle at around $1.33 R_V$ along the subsolar point (see panel d). Even though the solar wind
196 dynamic pressure is higher than the ionospheric peak pressure, the magnetic field does not
197 penetrate into the ionosphere right away. In fact, simulation results show that the penetration of
198 the magnetic field into the ionosphere is a much slower process, taking nearly an hour to form a
199 magnetized ionosphere (panels e and f). The magnetic field gradually increases at lower altitude,
200 form a local maximum near the ionospheric thermal pressure peak and a local minimum above.
201 At the end of the pressure pulse, around 3 hour (see panel h), the peak magnetic pressure in the
202 ionosphere is about 60% of the peak value in the MPB region.

203
204 When the pressure pulse ends at the outer boundary and propagates to Venus around 03:01:40
205 (panel i), the dynamic pressure outside the bow shock drops back to 4.5 nPa, and the bow shock
206 location quickly moves outward from $1.32 R_V$ to $1.5 R_V$ (panels j and k). The peak magnetic
207 pressure in the IM and the thermal pressure in the magnetosheath region adjust rapidly back to
208 the new solar wind conditions. However, the magnetic field inside the ionosphere responds much
209 more slowly to the solar wind dynamic pressure variation. The magnetic field inside the
210 ionosphere slowly diffuses away (panel m, n). The fields inside the ionosphere are largely
211 horizontal “fossil fields,” existing more than 2 hours after the density pulse event (panel o).

212

213 The variations of electron number density and magnetic field in the ionosphere are shown in
 214 Figure 3 to further help us understand the ionospheric responses. Panels a-g illustrate how the
 215 magnetic field gradually penetrates into the ionosphere during high solar wind pressure
 216 enhancement. It takes about 10 more seconds (panel b and c) for the magnetic field to be
 217 enhanced above the ionosphere. The peak magnetic field reaches around 150 nT at 1h 2m, while
 218 the field inside the ionosphere is still nearly zero. The large pressure gradient force pushes the
 219 plasma downward, with downward convecting magnetic field flux. Because of the large ion-
 220 neutral collision frequency, the flow speed inside the ionosphere is extremely low (in the order of
 221 m/s), so the convection of the magnetic field flux is a slow process (panel d-g). Panels h-l show
 222 the electron number density and magnetic field strength variations along the subsolar line after
 223 the pressure pulse, as the fossil magnetic field in the ionosphere gradually diffuses away. It is
 224 important to note that as the magnetic field penetrates into the ionosphere, the density profiles
 225 were also significantly altered. We also checked the variation of the ion composition during the
 226 event, and found that below 250 km altitude, the ion composition is quite steady.

227
 228 The evolution of the magnetic field in the ionosphere can be understood with the help of the
 229 magnetic induction equation

$$231 \frac{\partial \mathbf{B}}{\partial t} = \nabla \times (\mathbf{u} \times \mathbf{B}) - \nabla \times (\eta_m \nabla \times \mathbf{B}) \quad (1)$$

232
 233 where η_m is magnetic diffusivity. Based on equation (1), the change of magnetic field depends
 234 on two terms on the right side of the equation, corresponding to convection and
 235 diffusion/dissipation, respectively. As the magnetic field is mainly the horizontal component B_Y ,
 236 along the subsolar line, equation (1) can be simplified as:

$$237 \frac{\partial B_Y}{\partial t} = \frac{\partial}{\partial x} (\mathbf{V}_x B_Y) + \frac{\partial}{\partial x} (\eta_m \frac{\partial}{\partial x} B_Y) \quad (2)$$

238
 239 Panels 1b, 2b and 3b in Figure 4 show the vertical plasma flow (U_x) and magnetic resistivity
 240 (η_m) at 1 hour, 3 hour and 5 hour (solid lines), respectively. At high altitude, above 350 km, the
 241 magnetic diffusivity is small, so the magnetic field is mainly controlled by the convection term,
 242 and is basically frozen-in with the plasma. At very low altitude (below 140 km), the plasma flow
 243 is nearly zero, so the diffusion term plays the major role. Even though the vertical plasma flow in
 244 between 140 km and 350 km is quite small, normally less than 100 m/s, it has quite complicated
 245 patterns and also slowly changes due to different solar wind forcing. For quiet solar wind
 246 conditions (see panel 1b), at high altitude (> 300 km altitude), the magnetic pressure gradient and
 247 thermal pressure gradient forces are roughly balanced with each other, with a small upward
 248 pressure gradient force, so that downward moving solar wind protons are further decelerated. The
 249 plasma flow is fully stopped at around 300 km altitude, and planetary plasma between 240-300
 250 km altitude is moving upward due to upward pressure gradient force. Below 240 km altitude,
 251 downward gravity exceeds the pressure gradient force, which accelerates the plasma downward.
 252 This downward flow reaches a local maximum near 200 km altitude, because below the exobase,
 253 collisions between ions and neutrals significantly slow down the ion motion. This local peak of
 254 the downward plasma flow predicted by our 3D model is quite similar to what was calculated by
 255 *Cravens et al.* [1984] (Figure 1) using a 1D multi-species MHD model. The differences at high
 256 altitude are mostly due to the fact that the 1D model imposes an artificial upper boundary (at ~500
 257 km altitude). Also note that the downward plasma flow speed can be up to a few km/s near 400

258 km altitude, much larger than the ~ 10 m/s used in the upper boundary of the 1D model at 500 km
259 altitude, which could partly explain the density difference from the 1D model and PVO
260 observations [Shinagawa *et al.*, 1987].

261
262 The complicated flow patterns basically determine how the magnetic field evolves with time in
263 the subsolar ionosphere. At 3 hour, due to high solar wind pressure, the downward plasma flow is
264 never fully stopped by the ionospheric thermal pressure gradient force, providing continuous
265 downward supply of the magnetic flux from the high altitude. The magnetic field has a local
266 minimum around 240 km altitude, where the downward flow has a local peak. This is because the
267 magnetic fluxes should be conserved, meaning that $V_X B_Y$ should be a constant, and thus a local
268 maximum of $|V_X|$ results in a local minimum of $|B_Y|$. (Note that both V_X and B_Y are negative
269 values in the coordinate used). At 5 hour, the plasma condition is fairly similar to 1 hour, except
270 that between 150-210 km altitude, there is some remaining magnetic field that was formed during
271 the high-pressure pulse. Simulation results show that at 5 hour (panel 3a), 2 hours after the solar
272 wind returns to normal, the magnetic field in the ionosphere ~ 200 km altitude is still about 40 nT.
273 It has been suggested by *Luhmann et al.* [1983] that a large-scale magnetic field could have an
274 effect on the ionosphere and should be included in the ionospheric models. Our results show
275 that those “fossil” magnetic fields in the ionosphere indeed act as an additional obstacle to the
276 solar wind (as shown in panel 3b), help to further slowdown the shocked solar wind, and alter the
277 density and pressure in the ionosphere (see panels 3a and 3c). Model results clearly show that the
278 state of the ionosphere not only depends on the current solar wind condition, but is a complex
279 function of past solar wind conditions, similar to Titan and Mars [*Bertucci et al.*, 2008; *Ma et al.*,
280 2009; 2014].

281 282 **4. Discussion and summary**

283 We performed a time-dependent simulation to examine the response of the near-Venus space to a
284 dynamic pressure (density) enhancement of the solar wind. Simulation results show that the
285 intrinsic time scales for different plasma regions such as the ionosphere and induced
286 magnetosphere are very different. It takes less than ~ 2 minutes for the magnetosheath and the
287 induced magnetosphere to respond to solar wind pressure variations, but the response time of the
288 ionosphere is over a much longer time scale of at least hours. The study also shows that the total
289 ion escape rate increases with solar wind dynamic pressure, but not linearly due to the long
290 internal response time of the ionosphere.

291
292 The simulation results also reveal the controlling processes of the formation and evolution of the
293 large-scale magnetic field in the ionosphere. The large-scale magnetic fields form gradually in the
294 ionosphere during the high-solar wind dynamic pressure period via downward convection of the
295 plasma and associated magnetic flux. After the solar wind pressure drops to below the value of the
296 peak ionospheric thermal pressure, there is no more supply of magnetic flux from above, so the
297 magnetic field gradually decreases through diffusion. In addition, we find that those “fossil”
298 magnetic fields also play important roles in the ionosphere dynamics and can act as additional
299 obstacles to the shocked solar wind plasma. Thus, the state of the ionosphere not only depends on
300 the current solar wind condition, but is a complex function of the past solar wind condition. These
301 large-scale fields may also be twisted to form flux ropes, as suggested by *Russell et al.* [2013], and
302 will be the subject to future studies. In this study, we have only focused on a particular change in
303 the solar wind, namely solar wind density pulses. The system response to other types of solar

304 changes (e.g., solar minimum EUV conditions) and solar wind disturbances are also of interest
305 and will be the subject of future studies.

306

307 **Acknowledgments**

308 This work was supported by NASA's Solar System Working Program. Resources supporting this
309 work were provided by the NASA High-End Computing (HEC) Program through the NASA
310 Advanced Supercomputing (NAS) Division at Ames Research Center. The BATS-RUS code is
311 publicly available from <http://csem.engin.umich.edu/tools/swmf>. Simulation results can be
312 obtained at

313 https://agudata.epss.ucla.edu/AGUDATA_FROM_CALLISTO/2020_GRL_Venus_pubdata/.

314

315 **II. References**

316

317 Bertucci, C., et al. (2008), The magnetic memory of Titan's ionized atmosphere, *Science*, **321**,
318 1475

319 Brace, L. W., W. T. Kasprzak, H. A. Taylor, R. F. Theis, C. T. Russell, A. Barnes, J. D. Mihalov,
320 and D. M. Hunten (1987), The ionotail of Venus: Its configuration and evidence for ion
321 escape, *J. Geophys. Res.*, **92**, 15–26.

322 Cloutier, P. A. (1984). Formation and dynamics of large-scale magnetic structures in the
323 ionosphere of Venus. *J. Geophys. Res.*, 89(A4), 2401– 2405.
324 doi:10.1029/JA089iA04p02401.

325 Cravens, T.E., Shinagawa, H. and Nagy, A.F. (1984), The evolution of large-scale magnetic
326 fields in the ionosphere of Venus. *Geophys. Res. Lett.*, 11: 267-270.
327 doi:10.1029/GL011i003p00267

328 Cravens, T.E. (2013). The Solar Wind Interaction with Non-Magnetic Bodies and the Role of
329 Small-Scale Structures. In *Solar System Plasma Physics* (eds. J.H. Waite, J.L. Burch and
330 R.L. Moore). doi:10.1029/GM054p0353.

331 Edberg, N. J. T., et al. (2011), Atmospheric erosion of Venus during stormy space weather, *J.*
332 *Geophys. Res.*, 116, A09308, doi:10.1029/2011JA016749.

333 Elphic, R. C., C. T. Russell, J. A. Slavin, and L. H. Brace, Observations of the dayside ionopause
334 and ionosphere of Venus, *J. Geophys. Res.*, 85, 7679-7696, 1980.

335 Fedorov, A., Barabash, S., Sauvaud, J.-A., Futaana, Y., Zhang, T. L., Lundin, R., and Ferrier,
336 C. (2011), Measurements of the ion escape rates from Venus for solar minimum, *J.*
337 *Geophys. Res.*, 116, A07220, doi:10.1029/2011JA016427.

338 Luhmann, J. G., Elphic, R. C., Russell, C. T., Mihalov, J. D., & Wolfe, J. H. (1980).
339 Observations of large scale steady magnetic fields in the dayside Venus ionosphere.
340 *Geophys. Res. Lett.*, 7: 917-920. doi:10.1029/GL007i011p00917.

341 Luhmann, J. G., Elphic, R. C., Russell, C. T., Brace, L. H., & Hartle, R. E. (1983). Effects of
342 large-scale magnetic fields in the Venus ionosphere. *Adv. Space Res.*, 2(10), 17-21.

343 Luhmann, J. G., Russell, C. T., & Elphic, R. C. (1984). Time scales for the decay of induced
344 large-scale magnetic fields in the Venus ionosphere. *J. Geophys. Res.*, 89, 362-368.

345 Luhmann, J. G., Kasprzak, W. T., & Russell, C. T. (2007). Space weather at Venus and its
346 potential consequences for atmosphere evolution. *J. Geophys. Res.*, **112**, E04S10.

347 Ma, Y. J., et al. (2009), Time-dependent global MHD simulations of Cassini T32 flyby: From
348 magnetosphere to magnetosheath, *J. Geophys. Res.*, 114, A03204,
349 doi:10.1029/2008JA013676.

350 Ma, Y. J., Fang, X., Nagy, A. F., Russell, C. T., and Toth, G. (2014), Martian ionospheric
351 responses to dynamic pressure enhancements in the solar wind, *J. Geophys. Res. Space*
352 *Physics*, 119, 1272–1286, doi:10.1002/2013JA019402.

353 Ma, Y. J., Nagy, A. F., Russell, C. T., Strangeway, R. J., Wei, H. Y., & Toth G. (2013). A global
354 multispecies single-fluid MHD study of the plasma interaction around Venus. *J. Geophys.*
355 *Res. Space Physics*, 118, 321–330, doi:10.1029/2012JA018265.

356 Villarreal, M. N., Russell, C. T., Wei, H. Y., Ma, Y. J., Luhmann, J. G., Strangeway, R. J., &
357 Zhang, T. L. (2015). Characterizing the low-altitude magnetic belt at Venus:
358 Complementary observations from the Pioneer Venus Orbiter and Venus Express. *J.*
359 *Geophys. Res. Space Physics*, 120, 2232–2240, doi:10.1002/2014JA020853.

360 McComas, D. J., Spence, H. E., Russell, C. T., & Saunders, M. A. (1986). The average magnetic
361 field draping and consistent plasma properties of the Venus magnetotail. *Geophys. Res.*
362 *Lett.*, **91**, 7939.

363 Phillips, J. L., & Russell, C. T. (1987). Upper limit on the intrinsic magnetic field of Venus. *J.*
364 *Geophys. Res.*, 92(A3), 2253–2263. doi: 10.1029/JA092iA03p02253.

365 Romanelli, N., DiBraccio, G., Modolo, R., Leblanc, F., Espley, J., Gruesbeck, J., et al.
366 (2019). Recovery timescales of the dayside Martian magnetosphere to IMF
367 variability. *Geophysical Research Letters*, 46, 10977–
368 10986. <https://doi.org/10.1029/2019GL084151>

369 Russell, C. T., J. G. Luhmann, and R. C. Elphic, The properties of the low altitude magnetic belt
370 in the Venus ionosphere, *Adv. Space Res.*, 2(10), 13-16, 1983.

371 Russell, C.T. (2013). Magnetic Flux Ropes in the Ionosphere of Venus. In *Physics of Magnetic*
372 *Flux Ropes* (eds. C.T. Russell, E.R. Priest and L.C. Lee). doi:10.1029/GM058p0413.

373 Shinagawa, H., Cravens, T. E., and Nagy, A. F. (1987), A one-dimensional time-dependent
374 model of the magnetized ionosphere of Venus, *J. Geophys. Res.*, 92(A7), 7317– 7330,
375 doi:10.1029/JA092iA07p07317.

376 Shinagawa, H., and Cravens, T. E. (1988), A one-dimensional multispecies
377 magnetohydrodynamic model of the dayside ionosphere of Venus, *J. Geophys.*
378 *Res.*, 93(A10), 11263– 11277, doi:10.1029/JA093iA10p11263.

379 Shinagawa, H., Kim, J., Nagy, A. F. & Cravens, T. E. (1991). A comprehensive
380 magnetohydrodynamic model of the Venus ionosphere. *J. Geophys. Res.*, 96(A7), 11083–
381 11095. doi: 10.1029/90JA02505.

382 Shinagawa, H. (1996a). A two-dimensional model of the Venus ionosphere, 1. Unmagnetized
383 ionosphere. *J. Geophys. Res.*, 101(A12).

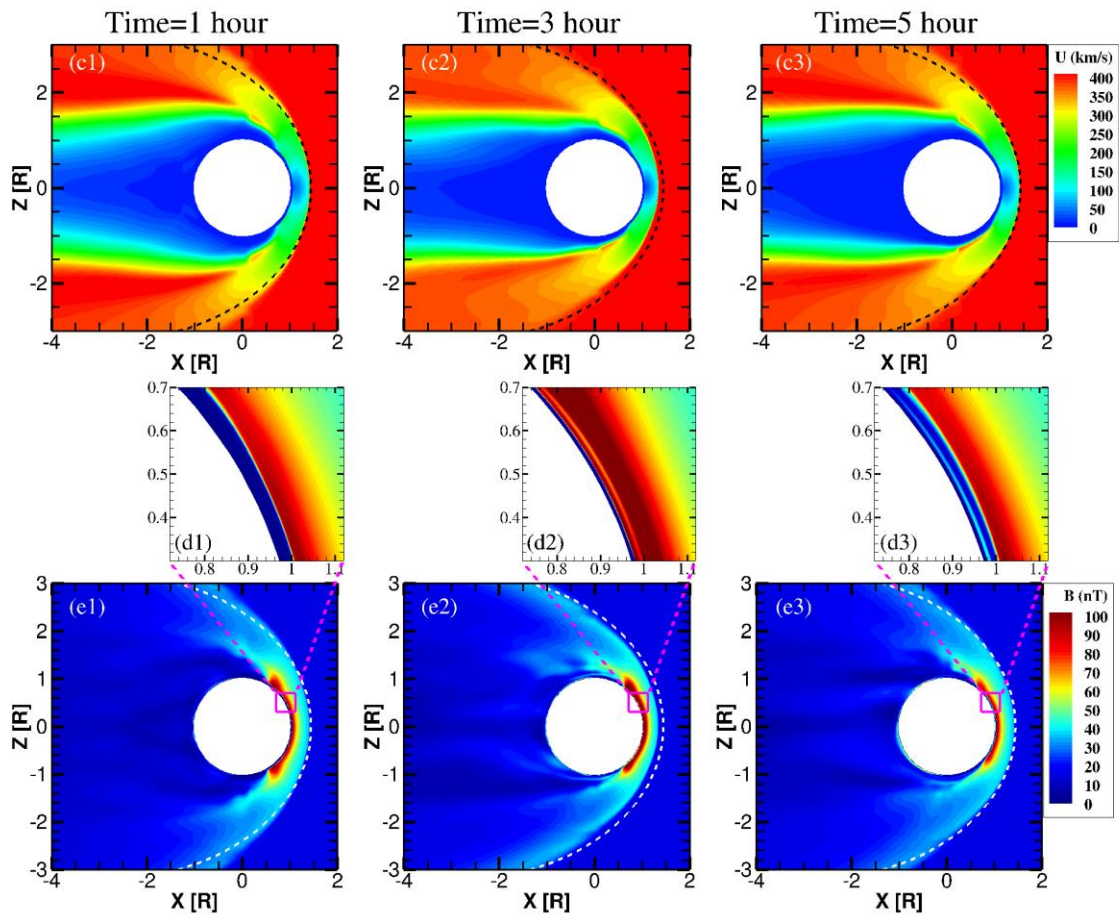
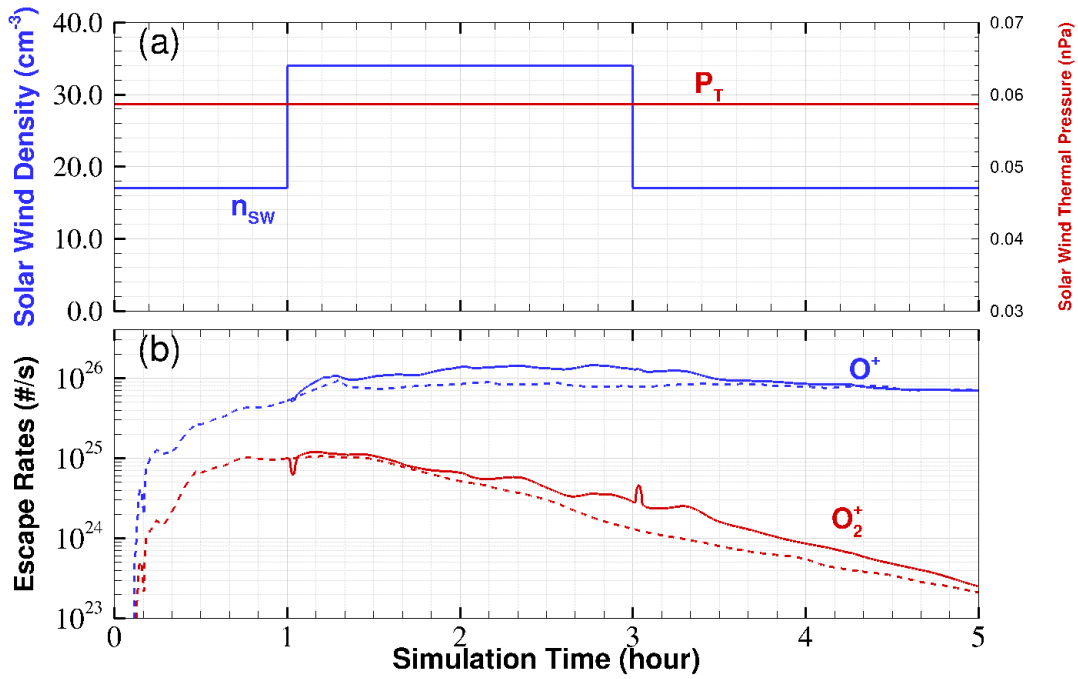
384 Shinagawa, H. (1996b). A two-dimensional model of the Venus ionosphere: 2. Magnetized
385 ionosphere, *J. Geophys. Res.*, 101(A12), 26921– 26930. doi:10.1029/96JA01362.

386 Tóth, G., et al. (2012), Adaptive Numerical Algorithms in Space Weather Modeling, *J. Comput.*
387 *Phys.*, 231, 870–903.

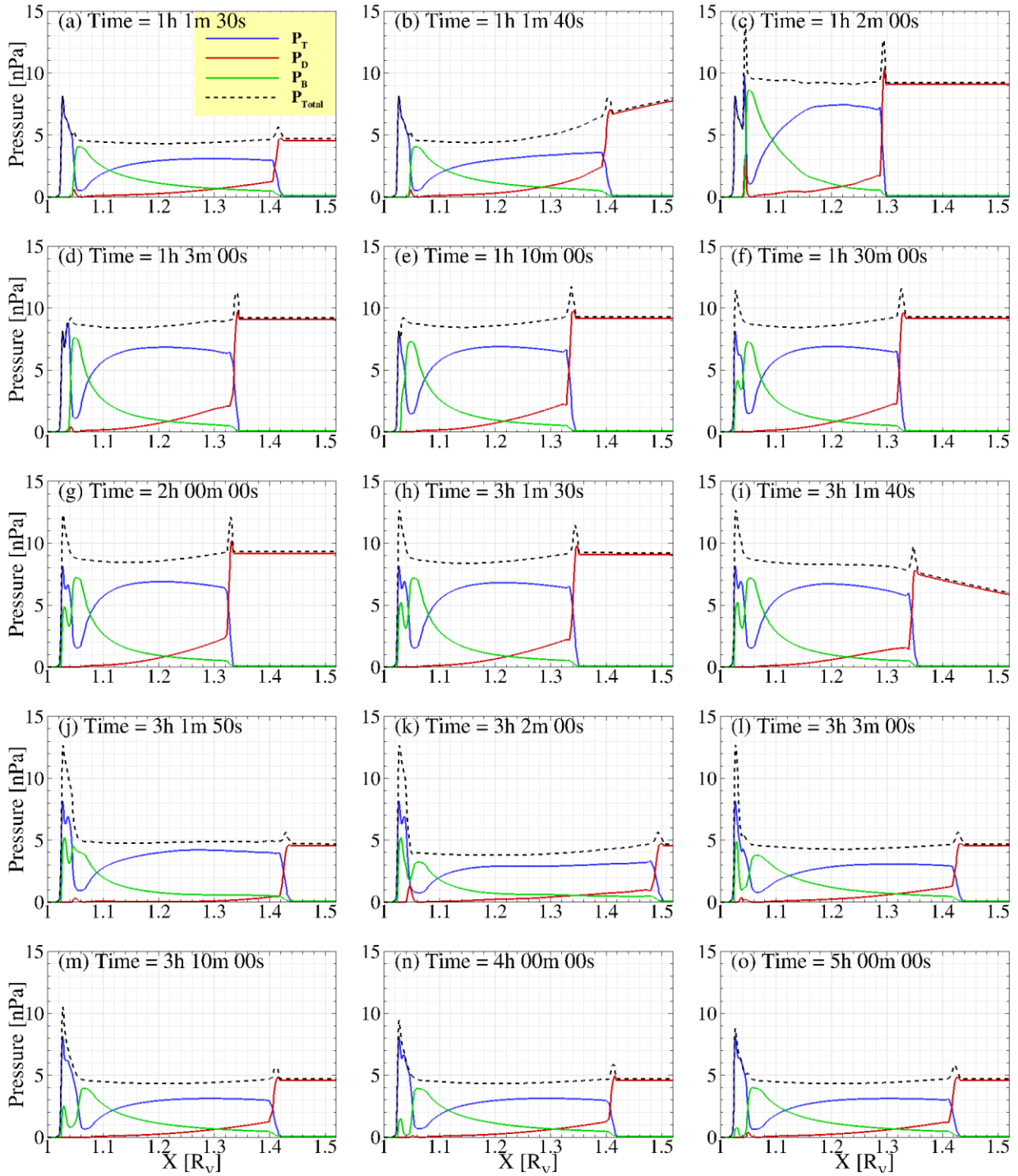
388 Villarreal, M.N., C.T. Russell, H.Y. Wei, Y.J. Ma, J.G. Luhmann, R.J. Strangeway, T.L.
389 Zhang, Characterizing the low-altitude magnetic belt at Venus: Complementary
390 observations from the Pioneer Venus Orbiter and Venus Express, *J. Geophys. Res.: Space*
391 *Physics*, 120, 3, 2232-2240, doi:10.1002/2014/JA020853, 2015

392 Zhang, T.-L., Luhmann, J.G., & Russell, C.T. (1990). The solar cycle dependence of the location
393 and shape of the Venus bow shock. *J. Geophys. Res.* **95**, 14961–14967.

394

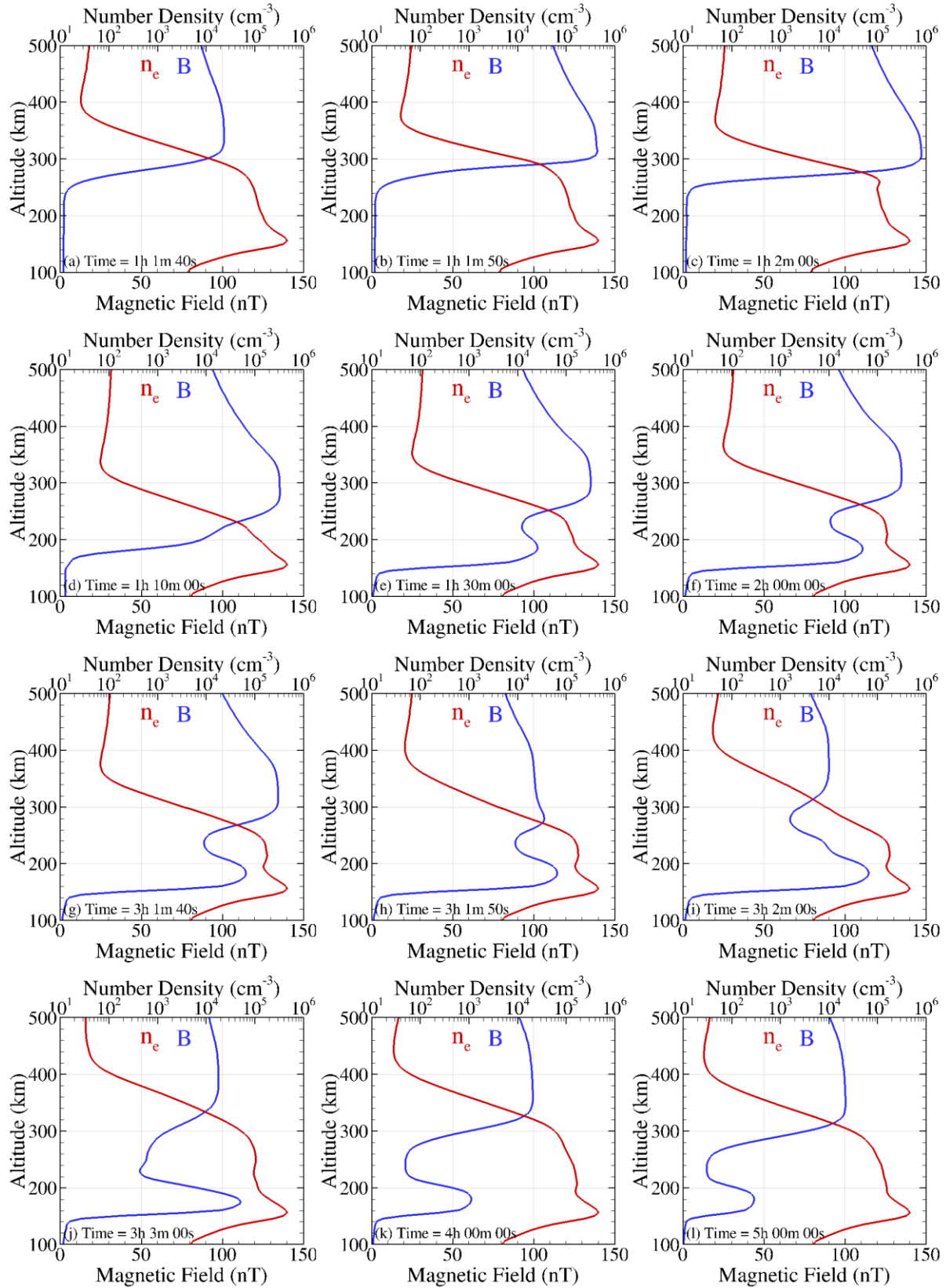


398 Figure 1. (a) Solar wind density and thermal pressure profiles used in the simulation. (b) ion
399 escape rates during the high-pressure pulse event (solid lines). The escape rates using quiet solar
400 wind conditions are shown in dashed lines for reference. Contour plots of plasma flow speed (c1-
401 c3) and magnetic field strength (e1-e3) in the XZ plane at 1 hour, 3 hour and 5 hour respectively.
402 The dashed curves show the average bow shock locations at solar maximum condition from
403 *Zhang et al.* [1990]. Zoom-in views of the magnetic field strength inside the purple region of
404 $0.72R_V < X < 1.12R_V$, and $0.3 R_V < Z < 0.7 R_V$ are shown in panels d1-d3.
405



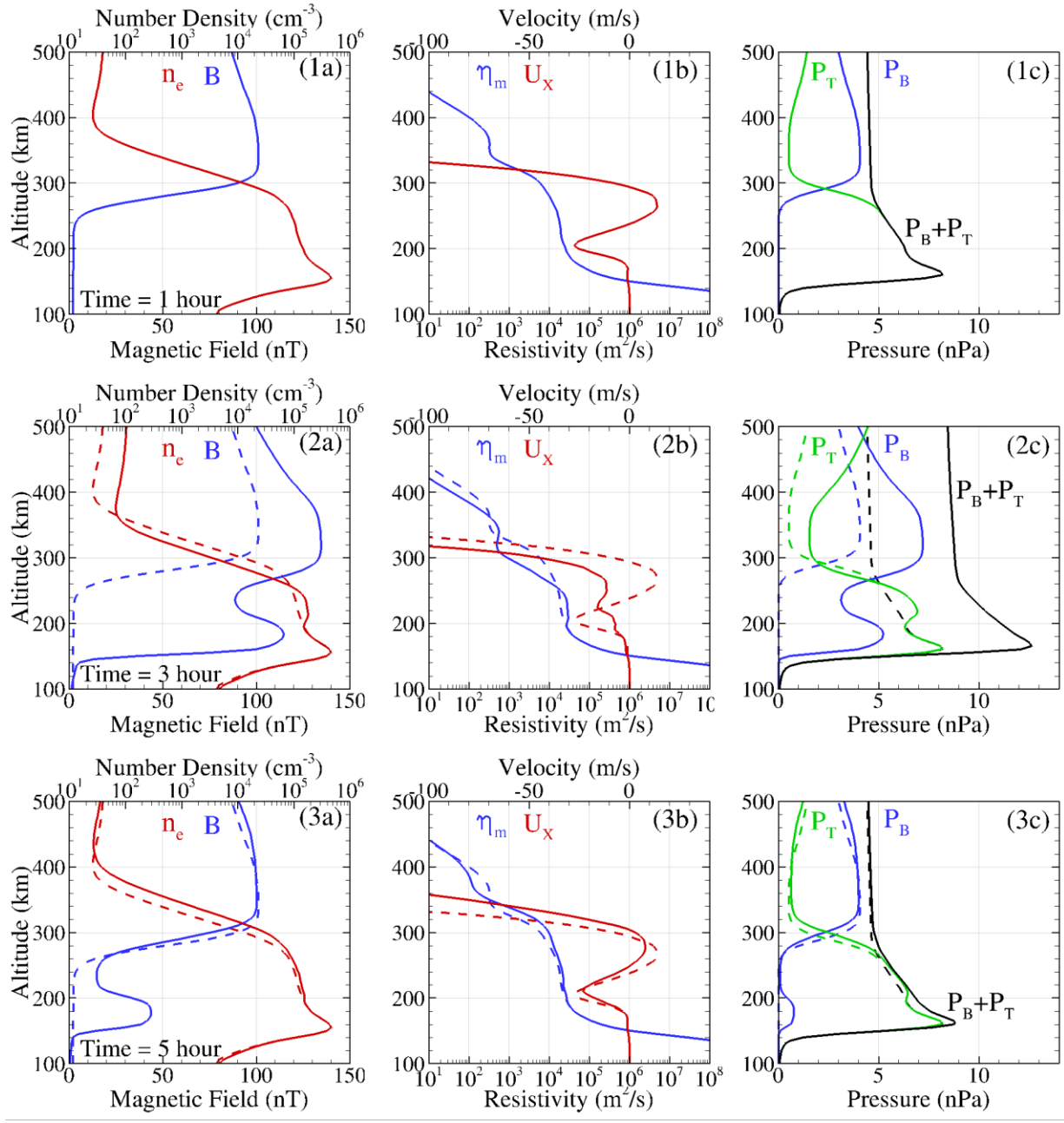
407
408
409
410
411
412

Figure 2. Snapshots of pressure profiles along the subsolar line during the solar wind density pulse event. Pressure profiles of thermal pressure (in blue), dynamic pressure (in red), magnetic pressure (green) and total pressure (black) are plotted in each panel.



413
414
415

Figure 3. Density and magnetic field responses to solar wind density variations along the subsolar line.



416
417
418
419
420

Figure 4. Plasma properties in the ionosphere of Venus at 1 hour, 3 hour and 5 hour. Dashed lines on the second and third rows are results at 1 hour for comparison.